

High-Efficiency Plasmonic Metamaterial Selective Emitter Based on an Optimized Spherical Core-Shell Nanostructure for Planar Solar Thermophotovoltaics

Lei Mo · Liu Yang · El Hang Lee · Sailing He

Received: 31 July 2014 / Accepted: 5 November 2014 / Published online: 18 November 2014
© Springer Science+Business Media New York 2014

Abstract We propose a high-efficiency plasmonic metamaterial selective emitter based on a tungsten (W) spherical core-shell nanostructure for potential applications in planar solar thermophotovoltaics. This structure consists of silicon dioxide (SiO₂)-coated W nanospheres periodically distributed on a W substrate and a thin W layer deposited on top. Using a new definition of spectral efficiency, numerical optimization is performed and its optical behaviors are systematically investigated. The numerical results show that our selective emitter has a high emissivity in the short wavelength range below the wavelength corresponding to the bandgap of the back photovoltaic cell and a low emissivity in the long wavelength range beyond it. Its spectral efficiency of 0.39 is much higher than those of other cases without the top W cover layer or the W nanospheres. Such excellent emission selectivity is attributed to the strong photonic interaction within the gaps between the adjacent core-shell nanospheres, the tightly confined optical fields in both the Ω -shaped W-SiO₂-W nanocavities, and the bottom nanocavities formed by the W nanospheres and the W substrate. It is also very tolerant toward the thicknesses of the SiO₂ layer and the top W cover layer.

Keywords Solar energy · Plasmonics · Metamaterial · Thermal emission

Introduction

Photovoltaics (PVs) are considered to be one of the most promising technologies to convert solar energy into electricity that can be used directly by human beings. It has attracted increasing attention in recent years. However, such PV cells have their own intrinsic limitations on power conversion efficiency, i.e., the Shockley-Queisser (SQ) limit [1], which results from two loss mechanisms. Sub-bandgap photons cannot be absorbed or converted to electrons. The photons with energy higher than the semiconductor bandgap will lose their extra energy through thermalization. Without considering the nonradiative recombination, the SQ limit of a single-junction solar cell with a bandgap of 1.0 eV is only 41 % for full concentration and only 30 % for non-concentration [1]. In order to overcome the SQ limit, multijunction solar cells, which connect two or more junctions of different bandgaps in sequence, have become the optimal choice [2]. Even though a high efficiency of 44.4 % has been realized [3], multijunction solar cells are not suitable for wide implementation due to their extremely high cost induced by the extreme vacuum conditions for semiconductor growth. Moreover, because of the serial configuration, its total current is determined by the minimal current generated by one of the sub-cells, as well as the lattice-mismatching-induced loss [4]. Dispersive concentration PVs, which split and concentrate sunlight onto different sub-cells with different bandgaps, are able to overcome the limitations of multijunction solar cells [3]. However, the spatially distributed sub-cells usually take up a lot of space, making this kind of PVs not very suitable to be implemented in dense cities [5]. Another potentially high-efficiency solar conversion system is a solar thermophotovoltaic (STPV)

L. Mo
Department of Physics, Zhejiang University, Hangzhou 310027,
People's Republic of China

L. Mo · L. Yang (✉) · E. H. Lee · S. He (✉)
Centre for Optical and Electromagnetic Research, State Key
Laboratory of Modern Optical Instrumentation, Zhejiang University,
Hangzhou 310058, People's Republic of China
e-mail: optyang@zju.edu.cn
e-mail: sailing@jorcep.org

S. He
Department of Electromagnetic Engineering, JORCEP, School of
Electrical Engineering, Royal Institute of Technology (KTH), S-100
44 Stockholm, Sweden

one [6, 7], where a selective absorber and selective emitter pair is inserted in front of a PV cell, serving the purpose of absorbing the broad solar radiation (via the selective absorber) and thermally emitting the bandgap photons through heat generated through sunlight absorption (via the selective emitter). The whole spectral energy of the solar radiation is compressed into photons with their energies well matching the semiconductor bandgap. In this case, all the solar radiation can be efficiently converted in the back PV cell. Theoretically, the ultimate efficiency of an STPV system is predicted to reach 85 % for full concentration and 54 % for non-concentration, far larger than the efficiency of traditional PVs determined by the SQ limit [7]. Nanophotonic STPV devices with efficiencies of over 3.2 % have been reported recently [8, 9]. The heat source from the sun in STPVs can also be replaced by other kinds of heat sources, e.g., thermal waste from factories. Then, STPVs become TPVs. In both STPVs and TPVs, a selective emitter is indispensable and plays a critically important role in the spectral selectivity of the thermal radiation so as to improve the overall power conversion efficiency of the system.

Early researches on selective emitters mainly focused on doping high-temperature materials with scarce rare earth oxides that emit optical radiations in certain luminescent bands [10–12]. However, it is usually very difficult to tune their radiation spectra other than by mixing suitable materials. In recent years, refractory materials, e.g., tungsten (W), and tantalum (Ta), have received increasing attention due to the developed nanophotonics and advanced nanofabrication technologies. Global optimization has been conducted to design selective absorbers and/or selective emitters [9, 13–16]. With a silicon/silica multilayer stack on a W slab [13], Lenert et al. fabricated the first nanophotonic STPV device [8]. Chester et al. proposed cermet emitters composed of nanoparticles of W and silicon dioxide (SiO_2) to achieve a thermal transfer efficiency of 75.59 % at 1000 K [14]. Photonic crystal emitters based on W [16–18] and Ta [9, 15] have been designed and fabricated. The radiation spectrum can be easily tuned by forming two-dimensional [9, 16, 17] or three-dimensional (3D) [18] patterns. A more appealing means to achieve selective radiance employs metamaterials, where both electric and magnetic resonances can be excited simultaneously [19]. Perfect absorption has been widely investigated. Its peak wavelength and bandwidth can be flexibly controlled through changing the shape or size of the composite unit structure [20]. According to Kirchhoff's law, the emissivity of a structure in thermal equilibrium is equal to its absorptivity at each wavelength [21]. Therefore, selective emitters can be easily realized with proper metamaterial designs. Liu et al. demonstrated the first metamaterial selective emitter based on a three-layer gold cross-dielectric-gold structure [22]. Wu et al. proposed a metamaterial-based integrated plasmonic absorber-emitter pair [23]. Epsilon-near-zero and epsilon-near-pole metamaterials have also been proposed to be used

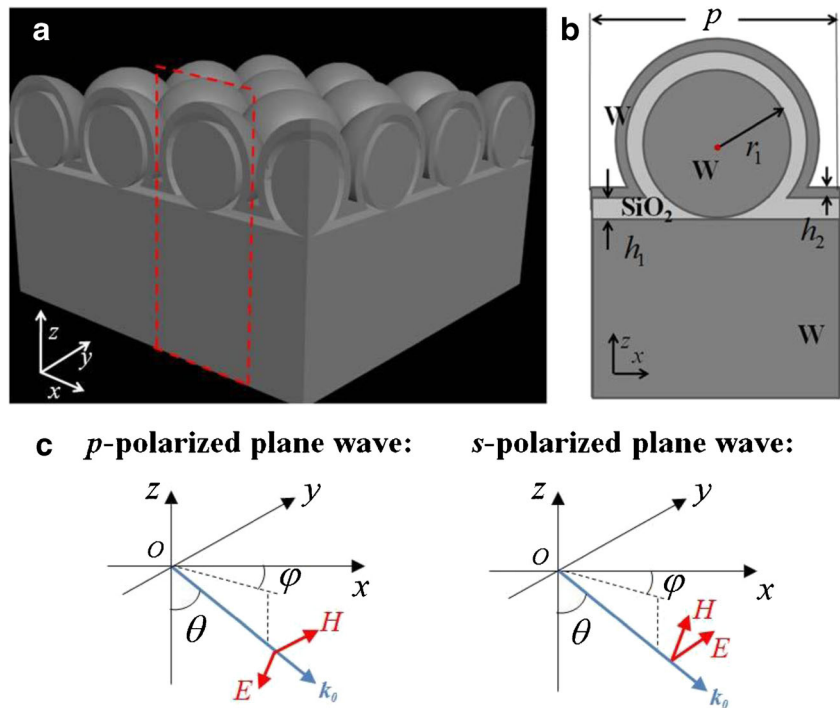
as selective emitters in TPVs [24]. So far, the few publications on metamaterial-based selective emitters [22–24] have already shown that metamaterials are one of the most promising ways to selectively control the radiation spectrum. However, the one reported in ref. [22] is a low-temperature selective emitter and is unsuitable for practical high-temperature STPV or TPV applications. The other two kinds of selective emitters [23, 24] are designed for cases with large emitter-to-absorber area ratios, which usually require very high operating temperatures (e.g., >1200 K) and a very high solar concentration, according to the global optimization of STPVs based on the detailed balance theory [25]. In contrast, for an optimized planar STPV system with equal areas of both the selective absorber and the selective emitter, its overall power conversion efficiency of 45.3 % can still surpass the SQ limit even though it is less than that of an optimized non-planar system [25]. In the fully optimized planar STPV system with a perfect backside reflector and a full emitter-to-cell view factor, the emitter operating temperature can be as low as 1060 K and the solar concentration be only 4.4 suns as long as the cut-off energy of the selective absorber and the bandgap energy of the back single-junction PV cell are fully optimized, i.e., 1.01 and 0.605 eV, respectively [25]. Such planar STPV systems do not require large spaces or critical operating conditions and are therefore more suitable for practical applications. However, no selective emitters based on metamaterials have been reported for planar STPVs.

The optimal STPV system has been studied systematically in ref. [25]. However, how to realize these optimized parameters/limits is not reported. Here in this paper, we propose a plasmonic metamaterial-based high-efficiency as well as highly selective emitter for potential planar STPV applications. Refractory W is chosen as the main material. In addition to its high melting point of 3695 K, W has intrinsic emission selectivity, that is, high emissivity in the wavelength range of 1.5–2.5 μm and low emissivity at wavelengths longer than 2.5 μm . Therefore, we can benefit from this property to easily obtain enhanced emissivity in the wavelength range below 2.5 μm with long-wavelength emission greatly suppressed, which is of critical importance for matching the emitter's radiation with the bandgap of the back PV cell in a STPV system.

Structure and Simulation Method

Our selective emitter is schematically shown in Fig. 1a, which consists of an array of periodically distributed spherical core-shell nanostructures on a W substrate. The featured spherical core-shell nanostructure is formed by uniformly depositing SiO_2 and W thin layers in sequence onto the surfaces of the W nanospheres and substrate. The SiO_2 -coated W nanospheres can be seen as the core and the top W layer as the shell. As

Fig. 1 **a** 3D and **b** cross-sectional schematic diagrams of our W selective emitter based on a spherical core-shell nanostructure. **c** *p*- and *s*-polarized plane waves are considered as the source incident from the top when the absorption spectra are calculated



shown in Fig. 1b, the *W* nanosphere radius, the period, the middle SiO₂ layer thickness, and the *W* cover layer thickness are labeled r_1 , p , h_1 , and h_2 , respectively. Such core-shell nanostructure is different from not only those employed in nanolasing/luminescence applications, e.g., gold/silica/dye core-shell nanoparticles [26], a cadmium sulfide/silica/silver core-shell nanowire [27], a silicon/silica/silver core-shell nanowire [28], but also those used in photovoltaic applications, e.g., our previously reported thin film solar cell based on an amorphous silicon/gold core-shell nanograting [29], a silver/amorphous silicon core-shell single-nanowire solar cell [30]. All those nanostructures are based on a metal-dielectric core-shell nanostructure, consisting of only one metallic nanostructure as either the core [26, 27, 30] or the shell [28, 29]. The metallic loss must be minimized to a fairly low level, but meanwhile, the optical field must be confined tightly in the active semiconducting materials so as to enhance lasing/luminescence [26–28] or absorption [29, 30] in it. In contrast, in order to enhance the thermal emission in the short wavelength range, we aim to confine the optical field in high-loss materials, i.e., *W* in this work. Therefore, our structure is designed quite differently, having distinct features in the electric field distribution, which is the key to enhance the thermal emission to be discussed in detail later.

Quantitative full-field electromagnetic simulations were conducted with the finite-difference time domain (FDTD) method by using the commercial software of Lumerical FDTD Solutions. We calculated the emissivity spectra of our selective emitter indirectly by obtaining its absorptivity

spectra first; the direct and indirect ways are equal according to Kirchhoff’s law. In the absorption simulations, both *p*- and *s*-polarized plane waves illustrated in Fig. 1c were considered as the source incident from the top shown in Fig. 1a. For the case of normal incidence, only *s*-polarized light was set because of the structural symmetry. Its wavelength, λ , ranges from 0.6 to 4.0 μm . Bloch boundaries were set along the *x* and *y* directions, while perfectly matched layers were treated in the *z* direction. Since the *W* substrate is thick enough to suppress any light transmission through it, a power monitor was set up before the source to record the reflection spectrum. Then, the absorptivity (which is also the emissivity), written as $\alpha(\lambda)$, can be easily obtained by subtracting the reflectivity from one. We use Eq. (1) below to calculate the partial emissivity:

$$\alpha(\lambda) = \frac{\iiint \frac{\pi c}{\lambda} \cdot \text{Im}(\varepsilon_w) |E|^2 dx dy dz}{\text{source power}} \tag{1}$$

where c is the speed of light in vacuum, $\text{Im}(\varepsilon_w)$ is the imaginary part of the dielectric constant of *W*, and $|E|$ is the amplitude of the electric field distribution. Changing the integrating region, the partial emissivity can be obtained. The spectral emittance, $\varepsilon(\lambda)$, is simply the product of the emissivity and the spectral emittance of an ideal blackbody, which is expressed by the Planck distribution:

$$\varepsilon_{\text{BB}}(\lambda) = \frac{2hc^2}{\lambda^5} \frac{1}{e^{hc/\lambda kT} - 1} \tag{2}$$

where h is Planck's constant, k is the Boltzmann constant, and T is the blackbody temperature, which is set to 1060 K here as optimized in ref. [25]. Therefore, $\varepsilon(\lambda)=\alpha(\lambda)\cdot\varepsilon_{\text{BB}}(\lambda)$ can be obtained.

In order to quantitatively characterize the performances of our proposed selective emitter, we define a more accurate spectral efficiency, η_{sp} , compared with that used in ref. [9]. It consists of two parts. One is written as η_t , the ratio of the thermal emission energy below the wavelength determined by the semiconductor bandgap, λ_{PV} , to the total thermal emission energy of the selective emitter, and is expressed in Eq. (3). It illustrates how well the emission in the long wavelength range of $\lambda>\lambda_{\text{PV}}$ could be suppressed. However, it cannot reflect how strong the emittance below the target bandgap is. Therefore, we define another parameter as η_c , the thermal emission ratio of the emitter to the blackbody below λ_{PV} , which is expressed in Eq. (4) below. Only when both of them are large can η_{sp} become large. Therefore, η_{sp} is defined as their product, expressed in Eq. (5).

$$\eta_t = \frac{\int_0^{\lambda_{\text{PV}}} \varepsilon(\lambda) d\lambda}{\int_0^{\infty} \varepsilon(\lambda) d\lambda} \quad (3)$$

$$\eta_c = \frac{\int_0^{\lambda_{\text{PV}}} \varepsilon(\lambda) d\lambda}{\int_0^{\lambda_{\text{PV}}} \varepsilon_{\text{BB}}(\lambda) d\lambda} \quad (4)$$

$$\eta_{\text{sp}} = \eta_t \eta_c \quad (5)$$

According to the fully optimized parameters [25], the bandgap of the back PV cell is 0.605 eV, corresponding to $\lambda_{\text{PV}}=2.06 \mu\text{m}$. Since the emitter's operating temperature is only 1060 K, the blackbody emission's cut-off energy is smaller than the optimized cut-off energy of the selective absorber, 1.01 eV, and eventually determines the smallest wavelength that the selective emitter can emit. Therefore, the spectral characteristics of our selective emitter around $\lambda_{\text{PV}}=2.06 \mu\text{m}$ are very critical and need to be carefully optimized.

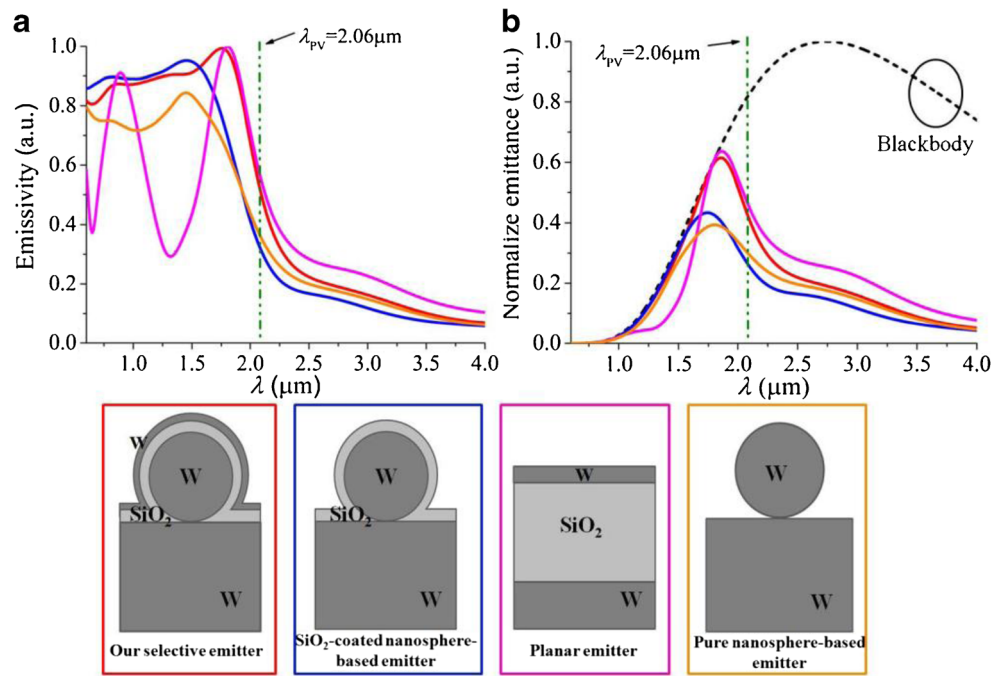
Results and Discussions

Based on the above methods, we performed a systematic optimization of our proposed selective emitter based on

spherical core-shell nanostructures by using η_{sp} as a figure of merit. The normally incident cases were considered until otherwise specified when calculating the absorption spectra (equal to the emissivity spectra). Figure 2a, b shows the emissivity and normalized emittance spectra (denoted as red curves), respectively, of our selective emitter, whose structural parameters are $r_1=130 \text{ nm}$, $h_1=25 \text{ nm}$, $h_2=30 \text{ nm}$, and $p=390 \text{ nm}$. These values are all optimized (and will be shown later), generating the highest spectral efficiency, i.e. $\eta_{\text{sp}}=0.39$ with $\eta_t=0.45$ and $\eta_c=0.87$, as indicated in Table 1. As shown in Fig. 2a, as the wavelength increases, the emissivity of our selective emitter slowly increases in the short wavelength range until $\lambda=1.75 \mu\text{m}$, where the spectrum peaks and beyond which it drops quickly. When $\lambda>\lambda_{\text{PV}}$, it becomes less than half of its maximum value. In Fig. 2b, in order to give a clear plot of the emittance spectrum, the blackbody emittance is normalized to its maximum (denoted as the black dashed curve). A normalized spectral emittance of our selective emitter is obtained and shown here by multiplying the emissivity spectrum shown in Fig. 2a with the normalized blackbody emittance. Due to the blackbody emittance peak lying in the range of $\lambda>\lambda_{\text{PV}}$, the emission of our selective emitter in this range is not well suppressed, thus leading to a relatively large η_t . Fortunately, the emittance in the short wavelength range is high enough, resulting in a very large value for η_c .

To demonstrate the importance of the W cover layer and the nanospheres, we calculated and optimized two other selective emitters using the same method. They are the SiO_2 -coated nanosphere-based emitter without the top W cover layer and the planar emitter without the W nanospheres as indicated in the inset of Fig. 2. Their emissivity and normalized emittance spectra are shown in Fig. 2a, b, respectively, with optimized structural parameters: $r_1=130 \text{ nm}$, $h_1=30 \text{ nm}$, and $p=400 \text{ nm}$ for the SiO_2 -coated nanosphere-based emitter (blue curves); and $h_1=420 \text{ nm}$ and $h_2=15 \text{ nm}$ for the planar emitter (pink curves). From Fig. 2a, it is seen that the emissivity spectra blue shifts more for the SiO_2 -coated nanosphere-based emitter than the other two cases, leading to the lowest η_c of 0.71, as indicated in Table 1. In order to show the role of SiO_2 coating in the SiO_2 -coated nanosphere-based emitter, we also calculated and optimized a pure nanosphere-based emitter without both top W cover layer and the SiO_2 coating, which is schematically shown in the inset of Fig. 2. Its optimal structural values are $r_1=140 \text{ nm}$ and $p=360 \text{ nm}$. Briefly, by comparing their emissivity spectra shown in Fig. 2a, one can see that the SiO_2 coating could greatly improve the emission performance through suppression of reflection in the short wavelength range, leaving the pure nanosphere-based emitter with much lower η_c of 0.64 as indicated in Table 1. Interference-induced ripples are observed for the planar emitter as shown in Fig. 2a. The dip in the emissivity spectrum means that the emitter is not fully emitting, also leading to a very low η_c of 0.73 in comparison with

Fig. 2 **a** Emissivity and **b** normalized emittance spectra of our selective emitter based on spherical core-shell nanostructures (red curves), the SiO₂-coated nanosphere-based emitter (blue curves), the planar emitter (pink curves), and the pure nanosphere-based emitter (orange curves), whose cross-sectional schematic diagrams are inserted below. The vertical green dash-dotted lines in the two figures mark the wavelength corresponding to the bandgap of the back PV cells, which is set to $\lambda_{PV}=2.06\ \mu\text{m}$. The black dashed curve in **b** represents the blackbody radiation at 1060 K normalized to its maximum



that of our selective emitter. In the long wavelength range of $\lambda > \lambda_{PV}$ as shown in Fig. 2b, the emittance of the SiO₂-coated nanosphere-based emitter is suppressed the most and the planar one the least. The values of η_t are 0.48 and 0.33, respectively. From Table 1, it is seen that our selective emitter can still obtain a high η_t of 0.45, not deviating much from that of the SiO₂-coated nanosphere-based emitter. By comparing all the optimized emitters, our selective emitter has the best overall performance, with the highest η_{sp} .

In order to further investigate its operating mechanism, we also plotted the electric field distributions at various typical wavelengths of the above-mentioned optimized selective emitters as shown in Fig. 3. For our selective emitter based on spherical core-shell nanostructures at the peak wavelength of $\lambda=1.75\ \mu\text{m}$ shown in Fig. 3(a1), an extremely strong electric field is localized in the gaps between adjacent core-shell nanospheres (the gap value is related to the period, the diameter of the nanospheres, the SiO₂ coating thickness, and the W cover layer thickness). At the same time, a strong electric field in an Ω shape can also be observed in the SiO₂ coating layer sandwiched by the W nanosphere and the W

cover layer, forming an Ω -shaped W-SiO₂-W nanocavity. Moreover, the electric field becomes much stronger at the bottom of the nanosphere, where there is a gradually decreasing distance between it and the bottom W substrate, forming another plasmonic nanocavity. These unique field characteristics contribute to the high emissivity shown in Fig. 2a. In comparison, without the W cover layer, the adjacent strong electric field becomes weakened and the Ω -shaped cavity mode also disappears, as shown in Fig. 3(b1) (though a strong electric field remains at the bottom of the nanosphere). Further removing the SiO₂ coating, the electric field becomes a little stronger in the gaps between adjacent nanospheres but much weaker in the bottom nanocavity as shown in Fig. 3(d1). Therefore, both the SiO₂-coated nanosphere-based emitter and the pure nanosphere-based emitter have lower emissivity at their peak wavelengths than our selective emitter, which is shown in Fig. 2a. For the planar emitter without the nanosphere, the Ω -shaped W-SiO₂-W nanocavity in our selective emitter becomes flat, and only Fabry-Perot resonances can be excited, as can be seen in Fig. 2a. Figure 3(c1) shows the first resonant electric field distribution with its maximum in the middle SiO₂ layer.

By blue shifting the emitting wavelength to $\lambda=1.3\ \mu\text{m}$, the originally strong electric field at the peak wavelength becomes much weaker for the three nanosphere-based emitters, namely our selective emitter, the SiO₂-coated nanosphere-based emitter, and the pure nanosphere-based emitter as shown in Fig. 3(a2), (b2), (d2), while at this wavelength, a destructive resonance appears in the planar emitter, as shown in Fig. 3(c2). This results in a lower emissivity for all the emitters as compared to the emissivity at their peak wavelengths, as

Table 1 Comparison of the spectral efficiencies of the four optimized selective emitters

	η_t	η_c	η_{sp}
Our selective emitter	0.45	0.87	0.39
SiO ₂ -coated nanosphere-based emitter	0.48	0.71	0.34
Planar emitter	0.33	0.73	0.24
Pure nanosphere-based emitter	0.41	0.64	0.26

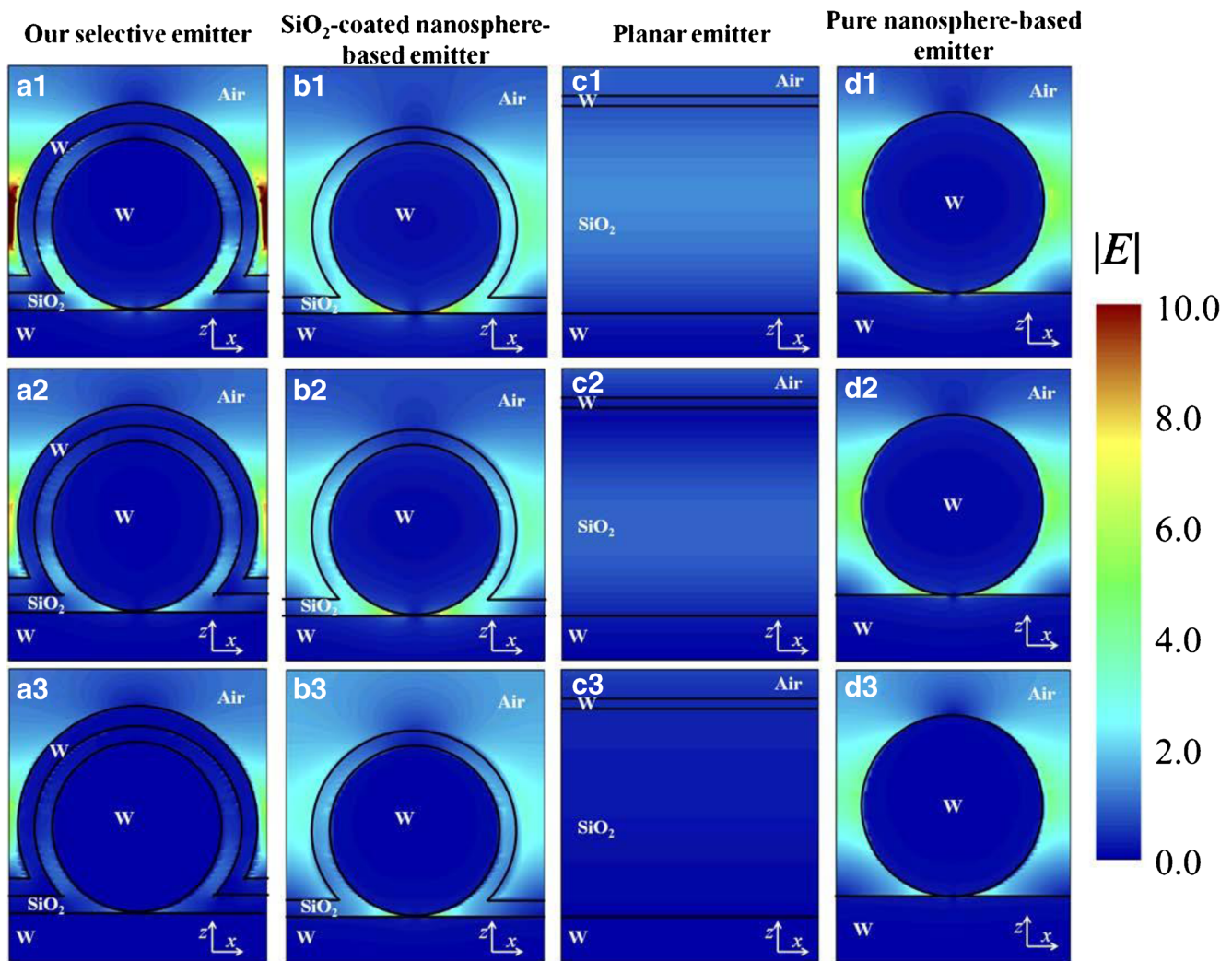


Fig. 3 Electric field distributions of *a1–a3* our selective emitter based on spherical core-shell nanostructures; *b1–b3* the SiO_2 -coated nanosphere-based emitter; *c1–c3* the planar emitter; and *d1–d3* the pure nanosphere-based emitter, at their peak wavelengths (i.e., $\lambda=1.75$, 1.46 , 1.8 , and

$1.45 \mu\text{m}$, respectively; *top row*). Their field distributions at a shorter wavelength (e.g., $\lambda=1.3 \mu\text{m}$; *middle row*) and a longer wavelength (e.g., $\lambda=3.0 \mu\text{m}$; *bottom row*) are also plotted for comparison

shown in Fig. 2a. On the other hand, when red shifting the emitting wavelength to $\lambda=3.0 \mu\text{m}$, where W is intrinsically highly reflective and thus weakly emissive, a much lower emissivity is achieved for the four emitters shown in Fig. 2a even though there is still some electric field being confined in them, as shown in Fig. 3(a3)–(d3). All the electric field distributions in Fig. 3 confirm that our selective emitter is superior to the other three kinds of emitters, and both the nanospheres and the top W cover layer play a critical role in the excellent spectral emittance selectivity.

As analyzed above, for our selective emitter, the entire plasmonic mode at the emissivity peak wavelength of $\lambda=1.75 \mu\text{m}$, as shown in Fig. 3(a1), is characterized by the strong electric field distributions localized in the gaps between adjacent core-shell nanospheres, in the Ω -shaped W- SiO_2 -W nanocavities, and in the bottom nanocavities formed by the W nanospheres and the W substrate. These unique features are

intertwined and their distinct roles in the emissivity spectrum seem quite difficult to distinguish. Nevertheless, since the field distribution is determined by the composite materials and their geometry, we attempted to analyze them indirectly through the partial emissivity spectra of all the composite metallic nanostructures, which were calculated and plotted in Fig. 4. From this figure, it is clearly seen that all the three composite nanostructures contribute to the total emissivity in the short wavelength range below λ_{PV} , with much higher emission from the top W cover layer than those from the W nanospheres and the W substrate. This indicates the dominant role of the W cover layer which accommodates the strong photonic interaction within the gaps between the adjacent core-shell nanospheres. Therefore, the total emissivity is greatly enhanced, leading to a very high η_c . However, in the long wavelength range beyond λ_{PV} , the emission of the W cover layer still dominates the total emission, negatively

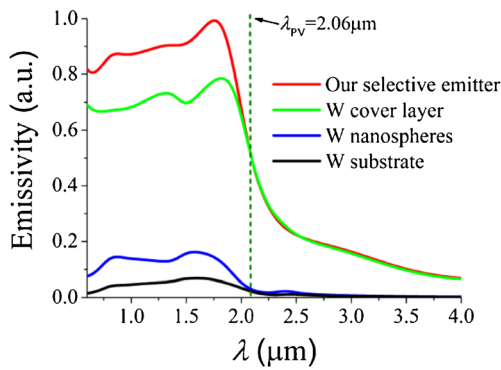


Fig. 4 Emissivity spectrum of our selective emitter based on spherical core-shell nanostructures (red curve) and its partial emissivity spectra of the W cover layer (green curve), the W nanospheres (blue curve), and the W substrate (black curve). The vertical green dashed line indicates the wavelength corresponding to the bandgap of the back PV cell

leading to a relatively low η_t . In contrast, there is nearly no emission from either the W nanospheres or the W substrate and thus the extremely weak electric fields localized in the Ω -shaped and the bottom nanocavities (shown in Fig. 3(c1)) play a positive role in the suppression of the emission in the long wavelength range. Fortunately, the η_{sp} is not influenced much due to the much higher enhancement of the emissivity in the short wavelength range.

For our selective emitter, the gaps between neighboring core-shell nanostructures play an important role in yielding high emissivity at the peak wavelength due to the confinement of the strongest electric fields in between as shown in Fig. 3(a1). This is reasonable and can be indicated by the dependence of the spectral efficiency, η_{sp} , on the period, p , which is shown in Fig. 5a. More accurately, η_c is strongly dependent on p , while

η_t is not as strongly dependent, indicating that the gaps between neighboring core-shell nanostructures do not severely influence the suppression of the emission in the long wavelength range of $\lambda > \lambda_{pv}$. When p increases from 390 nm, the gaps become larger, and the photonic interactions between the adjacent core-shell nanostructures become weaker. Consequently, the emissivity spectrum blue shifts, as shown in Fig. 5c. This behavior is quite different from a Bragg mode (which should red shift when p increases), indicating again that the localized surface plasmons in the gaps between adjacent core-shell nanostructures dominate the variation of the emissivity spectrum as shown in Fig. 5c. Therefore, η_c decreases as p increases. On the other hand, if p becomes too small, i.e., $p < 390$ nm, the neighboring core-shell nanostructures are nearly in contact with each other, and photons cannot easily be confined in those small gaps. Thus, the spectral emissivity is reduced (as shown in Fig. 5c), and η_c decreases as well. In this case, η_t also decreases because only a weak contrast appears in Fig. 5c between the short-wavelength emission and the long-wavelength suppression.

When changing the W nanosphere radius, r_1 , both the gaps between adjacent core-shell nanostructures and the bottom nanocavity formed by the W nanosphere and the W substrate will be changed, while the Ω -shaped W-SiO₂-W cavity does not change as the middle SiO₂ layer thickness is kept unchanged. When reducing r_1 from 130 nm, the photonic interactions within those cavities must be weakened, leading to a very weak field confinement. Therefore, it is seen in Fig. 5b that both η_{sp} and η_c decrease quickly from their maximum values. When r_1 becomes smaller than about 60 nm, both η_{sp} and η_c do not change much. In this case, the bottom field

Fig. 5 Spectral efficiency versus **a** the period, p , with $r_1 = 130$ nm and **b** the W nanosphere radius, r_1 , with $p = 390$ nm. **c, d** The variations of the corresponding spectral emissivity. The other structural parameters are $h_1 = 25$ nm and $h_2 = 30$ nm

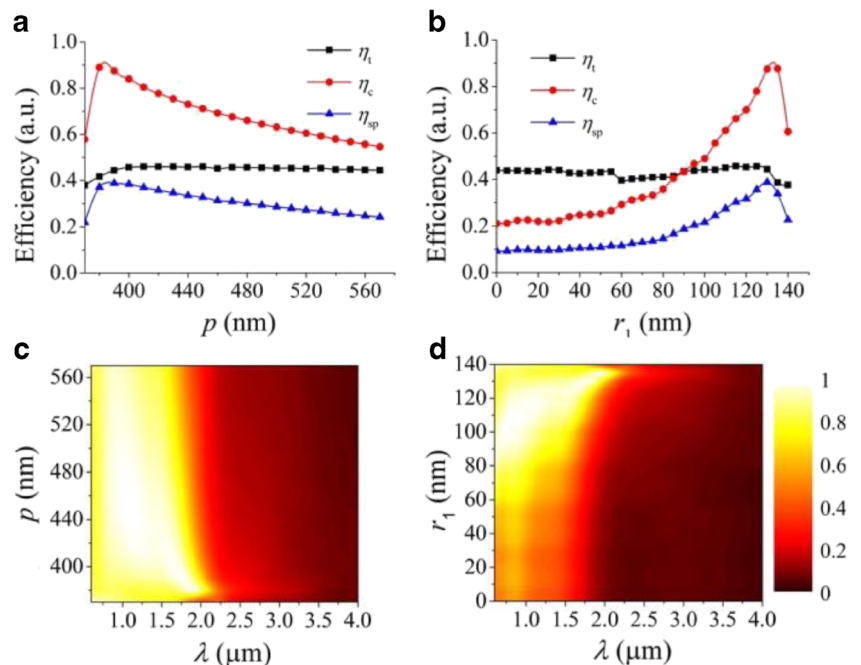
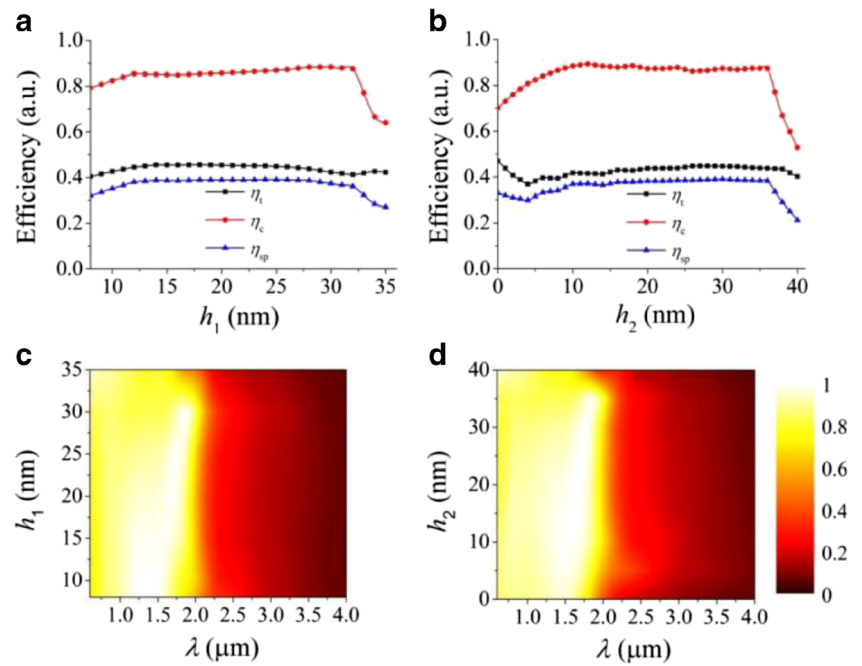


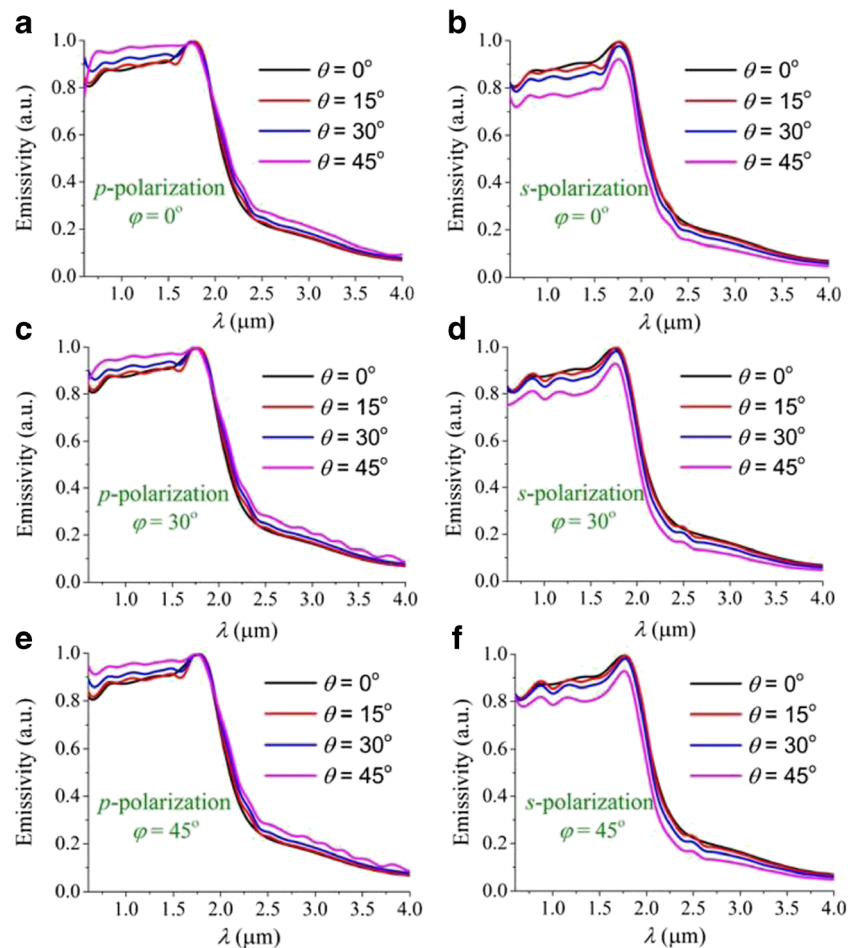
Fig. 6 Spectral efficiency versus **a** the SiO₂ thickness, h_1 , with $h_2=30$ nm and **b** the top W cover layer thickness, h_2 , with $h_1=25$ nm. **c, d** The spectral variations and corresponding emissivity. The other structural parameters are $r_1=130$ nm and $p=390$ nm



confinement dominates and becomes slightly weaker as r_1 decreases. From Fig. 5d, it is clearly seen that the spectrum

blue shifts, first quickly and then slowly where the emissivity becomes greatly weakened. Note that the first quick blueshift

Fig. 7 **a–f** Emissivity spectra at various typical elevation (θ) and azimuth (φ) angles for both p and s polarizations



of the emissivity spectrum vividly illustrates the major role of the localized photonic interaction between the adjacent core-shell nanospheres, while the slow blueshift shows the minor effect of the surface plasmons in the bottom nanocavities on the emissivity. This is consistent with the high partial absorption in the top W cover layer and the low partial absorption in the W nanospheres and the W substrate as shown in Fig. 4. When $r_1=0$, our selective emitter is reduced to a planar W-SiO₂-W three-layer structure with a SiO₂ layer thickness of only 25 nm. The narrow and weak emissivity spectrum in Fig. 5d confirms again the indispensable role of the nanospheres under the SiO₂ thin film. On the other hand, when r_1 increases to 140 nm, the neighboring core-shell nanospheres begin to touch each other. Similarly, η_{sp} , η_c , and η_t decrease, as shown in Fig. 5b.

In Fig. 6a, η_{sp} does not change much when h_1 ranges from 12 to 32 nm with other structural parameters kept unchanged. Beyond this range, η_{sp} decreases, dominated by the decreasing η_c in spite of the increasing η_t . Considering the field distribution, when h_1 increases, the SiO₂ layer becomes thicker, and longer wavelength photons can be confined tightly in the Ω -shaped W-SiO₂-W nanocavity. At the same time, the optical field confined in the gaps between adjacent core-shell nanospheres becomes stronger and eventually dominates the whole field distribution. Therefore, there is a rising trend for η_c , as shown in Fig. 6a. By further increasing h_1 , i.e., $h_1 > 32$ nm, the gaps between adjacent core-shell nanospheres become too narrow to accommodate any optical field, and thus the emissivity spectrum becomes lower and blue shifts, leading to lower values of η_c . Here, we did not consider the cases with $h_1 < 8$ nm, where quantum effects might exist and lead to complex optical responses [31]. In Fig. 6b, η_{sp} behaves similarly with h_2 as it does with h_1 . There is a nearly flat region with almost unchanged spectra when h_2 ranges from 10 to 36 nm, indicating that the emission performance is tolerant of h_2 . However, when h_2 is smaller than 10 nm, the optical field in the Ω -shaped W-SiO₂-W cavity becomes weakly confined, and the photonic interaction in the gaps between adjacent core-shell nanospheres also becomes weaker. On the other hand, when h_2 becomes larger than 36 nm, the gaps between adjacent core-shell nanospheres become too narrow to enable strong photonic interactions within it. Therefore, in the ranges of $h_2 < 10$ nm and $h_2 > 36$ nm, the emissivity is lower and the spectrum blue shifts as shown in Fig. 6d.

We also calculated the emissivity spectra at different elevation and azimuth angles for both p - and s polarizations. Some typical spectra were shown in Fig. 7. For p polarization, the emissivity peak does not change even when the elevation angle, θ , increases to 45° for different azimuth angles, namely, $\varphi=0^\circ$, 30°, and 45°. The emissivity increases in the short wavelength range as θ increases, and meanwhile, ripples appear in the long wavelength range as shown in Fig. 7a, c, e. With weak suppression of long wavelength emission, η_{sp}

decreases as θ increases for all azimuth angles. In contrast, for s polarization, the emissivity spectrum becomes lower as θ increases for different azimuth angles as shown in Fig. 7b, d, f. From these figures, it is seen that the emissivity of our selective emitter has a certain degree of divergence. Therefore, a relatively large PV cell is necessary to receive the emitted photons.

Conclusion

In conclusion, we have proposed a plasmonic metamaterial selective emitter based on W spherical core-shell nanostructures. Numerical optimization has been performed with the fully optimized parameters. In addition, its optical behaviors have been systematically analyzed. The numerical results have shown that our selective emitter has high emissivity in the short wavelength range of $\lambda < \lambda_{PV}$ and low emissivity in the long wavelength range of $\lambda > \lambda_{PV}$, leading to a higher spectral efficiency of $\eta_{sp}=0.39$, compared with the other cases without the top W cover layer or the W nanospheres. The optimized structure is very tolerant toward the SiO₂ coating layer thickness and the top W cover layer thickness. Such excellent emission performance is attributed to the strong photonic interaction within the gaps between adjacent core-shell nanospheres, the tightly confined optical field in both the Ω -shaped W-SiO₂-W nanocavities, and the bottom nanocavities formed by the W nanospheres and the W substrate. Therefore, our selective emitter is very promising for potential applications in planar STPVs or TPVs.

Acknowledgments This work was partially supported by the National Natural Science Foundation of China (Nos. 61307078, 91233208, and 91233119), the National High Technology Research and Development Program (863) of China (Nos. 2012AA030402 and 2013AA014401), the Zhejiang Provincial Key Project (No. 2011C11024), the Specialized Research Fund for the Doctoral Program of Higher Education and the Fundamental Research Funds for the Central Universities.

References

- Shockley W, Queisser HJ (1961) Detailed balance limit of efficiency of p-n junction solar cells. *J Appl Phys* 32:510–519
- Polman A, Atwater HA (2012) Photonic design principles for ultrahigh-efficiency photovoltaics. *Nat Mater* 11:174–177
- Green MA, Emery K, Hishikawa Y, Warta W, Dunlop ED (2014) Solar cell efficiency tables (version 43). *Prog Photovolt* 22:1–9
- Friedman DJ (2010) Progress and challenges for next-generation high-efficiency multijunction solar cells. *Curr Opin Solid State Mater* 14:131–138
- Barnett A, Kirkpatrick D, Honsberg C, Moore D, Wanlass M, Emery K, Schwartz R, Carlson D, Bowden S, Aiken D, Gray A, Kurtz S, Kazmerski L, Steiner M, Gray J, Davenport T, Buelow R, Takacs L, Shatz N, Bortz J, Jani O, Goossen K, Kiamilev F, Doolittle A,

- Ferguson I, Unger B, Schmidt G, Christensen E, Salzman D (2009) Very high efficiency solar cell modules. *Prog Photovolt* 17:75–83
6. Wedlockt B (1963) Thermo-photo-voltaic energy conversion. *Proc IEEE* 51:694–698
 7. Harder NP, Wurfel P (2003) Theoretical limits of thermophotovoltaic solar energy conversion. *Semicond Sci Tech* 18:S151–S157
 8. Lenert A, Bierman DM, Nam Y, Chan WR, Celanovic I, Soljačić M, Wang EN (2014) A nanophotonic solar thermophotovoltaic device. *Nat Nanotechnol* 9:126–130
 9. Rinnerbauer V, Lenert A, Bierman DM, Yeng YX, Chan WR, Geil RD, Senkevich JJ, Joannopoulos JD, Wang EN, Soljačić M, Celanovic I (2014) Metallic photonic crystal absorber-emitter for efficient spectral control in high-temperature solar thermophotovoltaics. *Adv Energy Mater* 4:1400334
 10. Chubb DL, Pal AT, Patton MO, Jenkins PP (1999) Rare earth doped high temperature ceramic selective emitters. *J Eur Ceram Soc* 19: 2551–2562
 11. Bitnar B, Durisch W, Mayor JC, Sigg H, Tschudi HR (2002) Characterisation of rare earth selective emitters for thermophotovoltaic applications. *Sol Energy Mater Sol Cells* 73:221–234
 12. Torsello G, Lomascolo M, Licciulli A, Diso D, Tundo S, Mazzer M (2004) The origin of highly efficient selective emission in rare-earth oxides for thermophotovoltaic applications. *Nat Mater* 3(9):632–637
 13. Rephaeli E, Fan S (2009) Absorber and emitter for solar thermophotovoltaic systems to achieve efficiency exceeding the Shockley-Queisser limit. *Opt Express* 17:15145–15159
 14. Bermel P, Ghebrebrhan M, Chan W, Yeng YX, Araghchini M, Hamam R, Marton CH, Jensen KF, Soljačić M, Joannopoulos JD (2010) Design and global optimization of high-efficiency thermophotovoltaic systems. *Opt Express* 18:A314–A334
 15. Nam Y, Yeng YX, Lenert A, Bermel P, Celanovic I, Soljačić M, Wang EN (2014) Solar thermophotovoltaic energy conversion systems with two-dimensional tantalum photonic crystal absorbers and emitters. *Sol Energy Mater Sol Cells* 122:287–296
 16. Chou JB, Yeng YX, Lenert A, Rinnerbauer V, Celanovic I, Soljačić M, Wang EN, King SG (2014) Design of wide-angle selective absorbers/emitters with dielectric filled metallic photonic crystals for energy applications. *Opt Express* 22:A144–A154
 17. Yeng Y, Ghebrebrhan M, Bermel P, Chan WR, Joannopoulos JD, Soljačić M, Celanovic I (2012) Enabling high-temperature nanophotonics for energy applications. *Proc Natl Acad Sci U S A* 109: 2280–2285
 18. Arpin KA, Losego MD, Cloud AN, Ning H, Mallek J, Sergeant NP, Zhu L, Yu Z, Kalanyan B, Parsons GN, Girolami GS, Abelson JR, Fang S, Braun PV (2013) Three-dimensional self-assembled photonic crystals with high temperature stability for thermal emission modification. *Nat Commun* 4:2063
 19. Landy NI, Sajuyigbe S, Mock JJ, Smith DR, Padilla WJ (2008) Perfect metamaterial absorber. *Phys Rev Lett* 100:207402
 20. Watts CM, Liu X, Padilla WJ (2012) Metamaterial electromagnetic wave absorbers. *Adv Mater* 24:OP98–OP120
 21. Rybicki GB, Lightman AP (1979) Radiative processes in astrophysics. John Wiley and Sons, New York
 22. Liu X, Tyler T, Starr T, Starr AF, Jokerst NM, Padilla WJ (2011) Taming the blackbody with infrared metamaterials as selective thermal emitters. *Phys Rev Lett* 107:045901
 23. Wu CH, Neuner B, John J, Milder A, Zollars B, Savoy S, Shvets G (2012) Metamaterial-based integrated plasmonic absorber/emitter for solar thermo-photovoltaic systems. *J Optics UK* 14:024005
 24. Molesky S, Dewalt CJ, Jacob Z (2013) High temperature epsilon-near-zero and epsilon-near-pole metamaterial emitters for thermophotovoltaics. *Opt Express* 21:A96–A110
 25. Datas A, Algora C (2013) Global optimization of solar thermophotovoltaic systems. *Prog Photovolt* 21:1040–1055
 26. Noginov MA, Zhu G, Belgrave AM, Bakker R, Shalaev VM, Narimanov EE, Stout S, Herz E, Suteewong T, Wiesner U (2009) Demonstration of a spaser-based nanolaser. *Nature* 460:1110–1112
 27. Cho CH, Aspetti CO, Turk ME, Kikkawa JM, Nam SW, Agarwal R (2011) Tailoring hot-exciton emission and lifetimes in semiconducting nanowires via whispering-gallery nanocavity plasmons. *Nat Mater* 10:669–675
 28. Cho CH, Aspetti CO, Park J, Agarwal R (2013) Silicon coupled with plasmon nanocavities generates bright visible hot luminescence. *Nat Photonics* 7:285–289
 29. Yang L, Mo L, Okuno Y, He S (2014) Optimal design of ultra-broadband, omnidirectional, and polarization-insensitive amorphous silicon solar cells with a core-shell nanograting structure. *Prog Photovolt* 21:1077–1086
 30. Zhan YH, Zhao JP, Zhou CH, Alemayehu M, Li YP, Li Y (2012) Enhanced photon absorption of single nanowire alpha-Si solar cells modulated by silver core. *Opt Express* 20:11506–11516
 31. Zuloaga J, Prodan E, Nordlander P (2009) Quantum description of the plasmon resonances of a nanoparticle dimer. *Nano Lett* 9:887–891